PhotoniX

RESEARCH Open Access

Terahertz spin-selective dielectric metasurfaces from exceptional points

Minggui Wei[1], Gui-Geng Liu[2], Yang Long[3], Zheyu Cheng[1], Song Han[4], Subhaskar Mandal[5] and Baile Zhang[1,6*]

*Correspondence:
blzhang@ntu.edu.sg

[1] Division of Physics and Applied Physics, School of Physical and Mathematical Sciences, Nanyang Technological University, 21 Nanyang Link, Singapore 637371, Singapore
[2] Department of Electronic and Information Engineering, School of Engineering, Westlake University, Hangzhou 310030, China
[3] School of Physics Science and Engineering, Tongji University, Shanghai 200092, China
[4] Innovative Institute of Electromagnetic Information and Electronic Integration, College of Information Science & Electronic Engineering, Zhejiang University, Hangzhou 310027, China
[5] Department of Physics, Indian Institute of Technology Bombay, Mumbai 400076, India
[6] Centre for Disruptive Photonic Technologies, The Photonics Institute, Nanyang Technological University, 50 Nanyang Avenue, Singapore 639798, Singapore

Abstract

Exceptional points (EPs) are spectral singularities where eigenvalues and eigenvectors coalesce, typically requiring complex couplings and enabling phenomena like unidirectional propagation. Meanwhile, metasurfaces, composed of artificially engineered arrays of subwavelength structures, enable unprecedented manipulation of electromagnetic waves. Recently, by tuning the coupling within a unit cell to realize an EP in the parameter space, metasurfaces with EPs have provided insights into the manipulation of light's spin states. However, metasurfaces with EPs based on complex couplings exhibit obvious residual zero-order diffraction in manipulating light's spin states. Here, we experimentally demonstrate a method to construct EPs in the parameter space without complex couplings within a unit cell, effectively suppressing residual zero-order diffraction. The EPs originate from the superposition of the accumulated phases from tailoring the sizes and relative rotation angles of the two pillars in a compound unit cell, forming nodal lines consisting of EPs in the parameter space. Using terahertz imaging technology, we experimentally observe spin-selective vortex beam generators and terahertz lenses constructed by metasurfaces with EPs in the parameter space. Our finding offers alternative insights to implement spin manipulation in metasurfaces and spin-dependent wavefront engineering devices.

Keywords: Exceptional points, Silicon metasurface, Terahertz

Introduction

Exceptional points (EPs), spectral degeneracies at which both eigenvalues and eigenstates coalesce in open systems under specific coupling conditions, have garnered considerable interest across diverse fields, including mechanics, acoustics, and optics [1–5]. Due to the coalescence of eigenstates at EPs, a variety of intriguing phenomena have emerged, including unidirectional wave propagation [6, 7], chiral absorption [8, 9], ultra-sensitive detection [10–12], and asymmetric reflection [13]. Meanwhile, metasurfaces, composed of arrays of spatially distributed subwavelength meta-atoms, have enabled versatile wavefront shaping [14–24], allowing for compact and efficient planar optical elements in various applications, e.g., polarization rotators [25, 26], waveplates [27], and q-plates [28, 29]. Recently, it has been reported that the eigenvalues and eigenvectors of the Jones matrix of a subwavelength unit cell can coalesce in parameter space by adjusting the coupling within the unit cell, leading to the emergence of an EP [30, 31]. Metasurfaces with EPs can implement intriguing

Springer

phenomena [32–34], e.g., pseudo-chirality [35] and extremely asymmetrical mirrors [36, 37]. Recently, metasurfaces with EPs have demonstrated full and independent control of polarization channels [38, 39], especially in manipulating light's spin states, for example, symmetrical spin state deflectors [31], asymmetric vectorial wavefront modulation [40], and arbitrarily polarized EPs [41]. However, metasurfaces with EPs based on complex couplings have shown obvious residual energy in the zero-order diffraction channel in spin-state manipulation.

In this study, we propose and experimentally demonstrate a method to implement EPs in the parameter space without complex couplings within a unit cell, effectively suppressing residual zero-order diffraction. The EPs arise from the superposition of phase contributions accumulated through geometric modulation of both the sizes and relative rotation angles of the two subwavelength dielectric pillars within a compound unit cell. Consequently, EPs form nodal lines in the parameter space. By utilizing terahertz field microscopy, we experimentally observe spin-selective terahertz vortex beam generators and lenses by EPs-enabled metasurfaces. Our results establish a robust framework for spin-dependent wavefront engineering and open new avenues for terahertz device design.

Methods

Figure 1 illustrates the schematic of dielectric spin-selective metasurfaces. The compound unit cell consists of two dielectric pillars (silicon) standing on a silicon substrate, as depicted in Fig. 1a. The compound unit cell has a height of $H=200$ μm, a thickness of $t=2$ mm, periods of $p_x=280$ μm along the x-direction, and $p_y=140$ μm along the y-direction, respectively. Meanwhile, a_1 and b_1 represent the length and width of the dielectric pillar on the left side, while a_2 and b_2 represent the length and width of the dielectric pillar on the right side, respectively. Each dielectric pillar has two axes, as denoted by x_r and y_r, respectively. The angles θ_1 and θ_2 are defined as orientation angles between the y_r-axis of the corresponding dielectric pillar and the y-axis, respectively, as shown in the lower panel of Fig. 1a. In general, the transmission or reflection characteristics of a dielectric pillar can be described by a Jones matrix, whose components represent the polarization conversion coefficients between incident and transmitted (or reflected) electric fields [15–18]. The transmission amplitude responses of a dielectric pillar's Jones matrix along the x_r- and y_r-axes are denoted as A_x and A_y under x and y-polarized incidence, while φ_x and φ_y are the corresponding phase responses, respectively. The transmission matrix of the compound unit cell can be written as the superposition of the transmission matrices associated with its two constituent dielectric pillars, as illustrated in Fig. 1b. To simplify our analysis, we set $A_x = A_y = A$ and $\varphi_x - \varphi_y = \pi$, which is a widely adopted condition in the metasurfaces [42–46]. Then, the transmission matrix of a compound unit cell, expressed on the spin basis with left-handed circular polarization (LCP) and right-handed circular polarization (RCP), can be simplified (See Note 1)

$$T_{cp} = A \begin{bmatrix} 0 & e^{i(\varphi_1 - 2\theta_1)} + e^{i(\varphi_2 - 2\theta_2)} \\ e^{i(\varphi_1 + 2\theta_1)} + e^{i(\varphi_2 + 2\theta_2)} & 0 \end{bmatrix} \tag{1}$$

where φ_1 and φ_2 are the phase responses (φ_x) of the corresponding dielectric pillars along the x_r-a xis, respectively. The spin conversion coefficients of the transmission matrix can be tuned by sweeping φ_1,φ_2,θ_1 and θ_2 in the parameter space. By

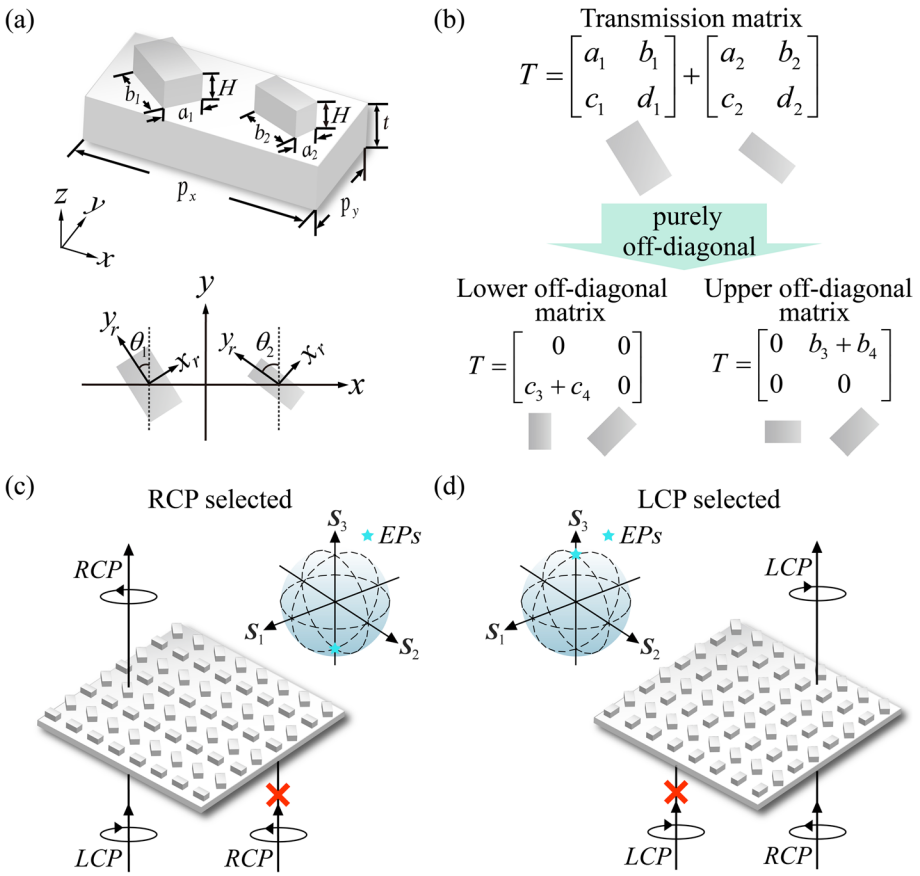

Fig. 1 Schematic of spin-selective dielectric metasurfaces. **a** Side (Upper panel) and top (Lower panel) views of a compound unit cell in the metasurface. The parameters are a height $H = 200$ μm, $t = 2$ mm, $p_x = 280$ μm, and $p_y = 140$ μm. a_1 and b_1 represent the length and width of the dielectric pillar on the left side, while a_2 and b_2 represent the length and width of the dielectric pillar on the right side. Each element has two axes, as denoted by x_r and y_r. The orientation angles θ_1 and θ_2 are defined as orientation angles between the y_r-axis of the dielectric pillars and the y-axis on the left and right side, respectively, as shown in the lower panel of **a**. **b** Schematic of a compound unit cell's transmission matrix transformed into a purely off-diagonal form by tailoring the sizes and adjusting the rotation angles of the two constituent dielectric pillars. **c** and **d** The schematic view of the spin-selective dielectric metasurfaces from sole conversion from LCP to RCP under the conditions $\varphi_1 = -\pi/4, \varphi_2 = \pi/4$ and $\theta_2 - \theta_1 = -\pi/4$(**c**), and sole conversion from RCP to LCP under the conditions $\varphi_1 = -\pi/4, \varphi_2 = \pi/4$ and $\theta_2 - \theta_1 = \pi/4$(**d**), respectively. LCP and RCP denote left-handed and right-handed circular polarization, respectively

tailoring the sizes and adjusting the rotation angles of the two constituent dielectric pillars, the compound unit cell's transmission matrix reduces to a purely off-diagonal form by eliminating $t_{12} = A/\sqrt{2}(e^{i(\varphi_1 - 2\theta_1)} + e^{i(\varphi_2 - 2\theta_2)})$ (from RCP to LCP) or $t_{21} = A/\sqrt{2}(e^{i(\varphi_1 + 2\theta_1)} + e^{i(\varphi_2 + 2\theta_2)})$ (from LCP to RCP) component, as illustrated by Fig. 1b. Consequently, the eigenvalues and eigenvectors of the transmission matrix coalesce, resulting in the emergence of EPs in the parameter space. The EPs in the parameter space originate from the coherent interference of the spin responses of the two constituent dielectric pillars in the compound unit cell. The eigenvectors of the transmission matrix correspond to the polarization states of the transmitted beams, which can be mapped onto the Poincaré sphere [31, 39, 40]. For example, as the eigenvectors of the transmission matrix coalesce and locate at the south pole of the Poincaré

sphere, sole conversion from LCP to RCP under the conditions $\varphi_1 = -\pi/4, \varphi_2 = \pi/4$ and $\theta_2 - \theta_1 = -\pi/4$ is schematic depicted in Fig. 1c. Figure 1d schematically shows that when $\theta_2 - \theta_1 = \pi/4$, only the RCP to LCP conversion remains, and the eigenvectors of the transmission matrix coalesce at the north pole of the Poincaré sphere.

Figures 2a and b depict the numerically calculated spin conversion coefficient t_{12} and t_{21} components in the parameter space with $\theta_1 \in [-\pi/2, \pi/2]$ and $\theta_2 \in [-\pi/2, \pi/2]$ under the condition $\varphi_1 = -\pi/4$ and $\varphi_2 = \pi/4$, respectively. When t_{12} or t_{21} component vanishes, the eigenvalues and eigenvectors of the transmission matrix coalesce, leading to the emergence of EPs in the parameter space. Notably, EPs form nodal lines in the

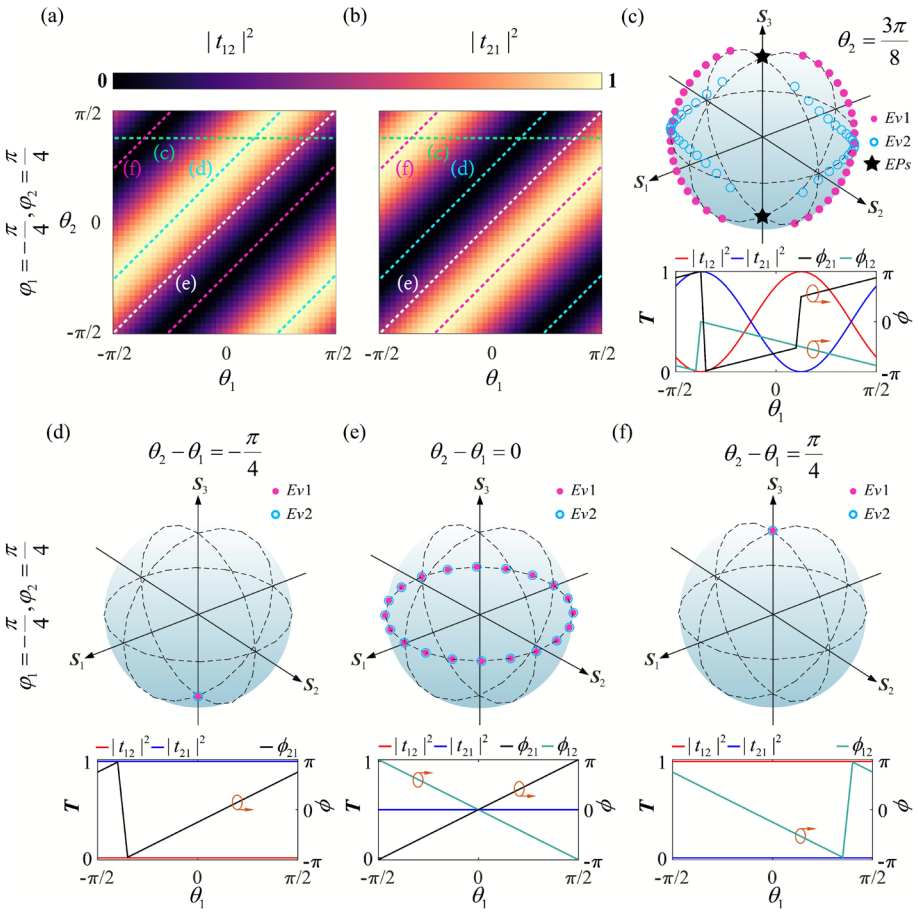

Fig. 2 Polarization states of the transmitted beams with different $\varphi_1, \varphi_2, \theta_1$ and θ_2 in the Poincaré sphere. **a** and **b** Simulated spin conversion coefficients t_{12} (**a**) and t_{21} (**b**) components in parameter space with $\theta_1 \in [-\pi/2, \pi/2]$ and $\theta_2 \in [-\pi/2, \pi/2]$ under the condition $\varphi_1 = -\pi/4, \varphi_2 = \pi/4$. φ_1 and φ_2 represent $\varphi_{x_i}(x, y)$ of dielectric pillars on the left and right sides in elements, respectively. The cyan dashed lines indicate two nodal lines corresponding to $N = 0$ and $N = 1$ in **a** and **b**, respectively. Meanwhile, the red dashed lines indicate two nodal lines corresponding to $M = 0$ and $M = -1$, respectively. The whites dashed lines indicate the case where $\theta_2 - \theta_1 = 0$. The green dashed lines indicate the case where θ_2 is $\theta_2 = 3\pi/8$ while θ_1 is varied. **c** The upper panel is the polarization states of the transmitted beams with $\varphi_1 = -\pi/4, \varphi_2 = \pi/4$, $\theta_2 = 3\pi/8$ at different θ_1 in the Poincaré sphere. The lower panel indicates the corresponding amplitude and phase responses for different components in the transmission matrix, respectively. **d** to **f** The upper panel shows the polarization states of the transmitted beams with $\varphi_1 = -\pi/4, \varphi_2 = \pi/4, \theta_2 - \theta_1 = -\pi/4$ (**d**), $\theta_2 - \theta_1 = 0$(**e**) and $\theta_2 - \theta_1 = \pi/4$(**f**) at different θ_1 in the Poincaré sphere, respectively. The lower panel indicates the corresponding amplitude and phase responses for t_{12} or t_{21} components in the transmission matrix, respectively

parameter space when the condition $\theta_2 - \theta_1 = \pi/4 + M\pi$ and $\theta_2 - \theta_1 = -\pi/4 + N\pi$ (M, $N \in Z$) is satisfied. There are two nodal lines corresponding to $N=0$ and $N=1$, as indicated by the cyan dashed lines in Fig. 2a and b, respectively. Meanwhile, there are two nodal lines corresponding to $M=0$ and $M = ^- 1$, as indicated by the red dashed lines in Fig. 2, respectively. The nodal lines cover the entire 2π phase range. Consequently, we can utilize compound unit cells with EPs to implement versatile phase profiles for spin-selective functionalities. The green dashed lines indicate the case where θ_2 is fixed to be $\theta_2 = 3\pi/8$ while θ_1 is varied, as depicted in Fig. 2a and b, respectively. The corresponding polarization states of the transmitted beams with $\varphi_1 = -\pi/4, \varphi_2 = \pi/4$ and $\theta_2 = 3\pi/8$ at different θ_1 on the Poincaré sphere in Fig. 2c. Ev_1 and Ev_2 are the eigenvectors of the transmission matrix. $\varnothing_{12}$ and $\varnothing_{21}$ represent the corresponding phase of t_{12} or t_{21}, respectively. The amplitude and phase responses for t_{12} or t_{21} components in the transmission matrix are depicted in Fig. 2c. EPs emerge at $\theta_1 = -3\pi/8$ on the south pole and $\theta_1 = \pi/8$ on the north pole of the Poincaré sphere, as indicated by black stars in Fig. 2c. The two eigenvectors of the transmission matrix do not coalesce and are distributed at different positions on the Poincaré sphere. The upper panel of Fig. 2d depicts the transmitted beams' polarization states with $\varphi_1 = -\pi/4, \varphi_2 = \pi/4$ and $\theta_2 - \theta_1 = -\pi/4$ at different θ_1 in the Poincaré sphere. In this case, the t_{12} component of the transmission matrix vanishes, resulting in coalesced eigenvalues and eigenvectors, which leads to the emergence of EPs in the parameter space, as depicted in the lower panel of Fig. 2d. Consequently, the transmitted beams' polarization states are located at the south pole in the Poincaré sphere, as illustrated in Fig. 2d. Only the conversion from LCP to RCP in the transmitted beam is allowed, while the conversion from RCP to LCP is forbidden, as schematically illustrated in Fig. 1c. At the same condition of $\varphi_1 = -\pi/4$ and $\varphi_2 = \pi/4$, t_{21} is equal to t_{12} when we set $\theta_2 - \theta_1 = 0$, as illustrated by whites dashed lines in Fig. 2a and b, respectively. The transmitted beams' polarization states are distributed on the equator of the Poincaré sphere when we vary θ_1, as illustrated in Fig. 2e. In this case, the conversion from RCP to LCP and vice versa in the transmitted beam is allowed. In contrast, when we set $\theta_2 - \theta_1 = \pi/4$, the transmitted beams' polarization states are located at the north pole of the Poincaré sphere as depicted in Fig. 2f. Consequently, only the conversion from RCP to LCP in the transmitted beam is allowed, while the conversion from LCP to RCP is forbidden, as schematically illustrated in Fig. 1d. Notable, when φ_1 and φ_2 vary, similar performance can still be achieved by appropriately adjusting the relative angle between θ_1 and θ_2. Consequently, by tuning θ_1, θ_2, φ_1 and φ_2 of the compound unit cells, we can engineer phase profiles $\varnothing_{12}$ and $\varnothing_{21}$ to realize different functionalities, such as vector beams and lenses, while simultaneously meeting the conditions for EPs in the parameter space.

Noticeable, when $\varphi_2 - \varphi_1 = (m+n)\pi/2$ and $\theta_2 - \theta_1 = (m-n)\pi/4$ (where m and n are odd integers), both t_{12} and t_{21} of the transmission matrix vanish. Consequently, transmission is not allowed when the incident spin state is either LCP or RCP. Specifically, when $\varphi_1 = \varphi_2$ (the two dielectric pillars are identical), the t_{12} and t_{21} components of the transmission matrix have equal amplitude but opposite phases, resulting in both components vanishing or remaining nonzero simultaneously. To achieve sole spin conversion, such as from LCP to RCP or vice versa, a metasurface composed of compound unit cells supporting EPs in the parameter space requires $\varphi_1 \neq \varphi_2$, providing a new strategy for

the manipulation of spin states. Additionally, the phase difference between φ_1 and φ_2 can influence the amplitudes of components in the transmission matrix, which directly contributes to applications for on-demand manipulation of the strength of spin states.

Results and discussion

Then, we design and fabricate spin-selective dielectric metasurfaces composed of compound unit cells that support EPs in the parameter space. Figure 3a depicts the schematic of the terahertz field scanning microscopy (See Note 2). As mentioned above, we can implement phase profiles $\varnothing_{12}$ or $\varnothing_{21}$ to generate vortex beams by adopting the parameters of θ_1, θ_2, φ_1 and φ_2 along the EP lines. Figures 3b to d illustrate the optical images of spin-selective vortex beam generators with $\Delta\varphi = \pi/2$ and $\Delta\theta = \pi/4$ (Fig. 3b), $\Delta\varphi = \pi/2$ and $\Delta\theta = 0$ (Fig. 3c), and $\Delta\varphi = \pi/2$ and $\Delta\theta = -\pi/4$ (Fig. 3d), respectively. The corresponding SEM images of fabricated microstructures for spin-selective vortex beam generators are depicted in Fig. 3e to g. Meanwhile, to investigate this wavefront phase encoding strategy, we design spin-selective lenses that are the fundamental optical elements widely utilized across various optical systems, e.g., telescope systems and microscopy. The optical images of spin-selective lenses with $\Delta\varphi = \pi/2$ and $\Delta\theta = \pi/4$ (Fig. 3h), $\Delta\varphi = \pi/2$ and $\Delta\theta = 0$ (Fig. 3i), and $\Delta\varphi = \pi/2$ and $\Delta\theta = -\pi/4$ (Fig. 3j), are depicted in Figs. 3h to j respectively. The numerical aperture and focal length are ~ 0.49

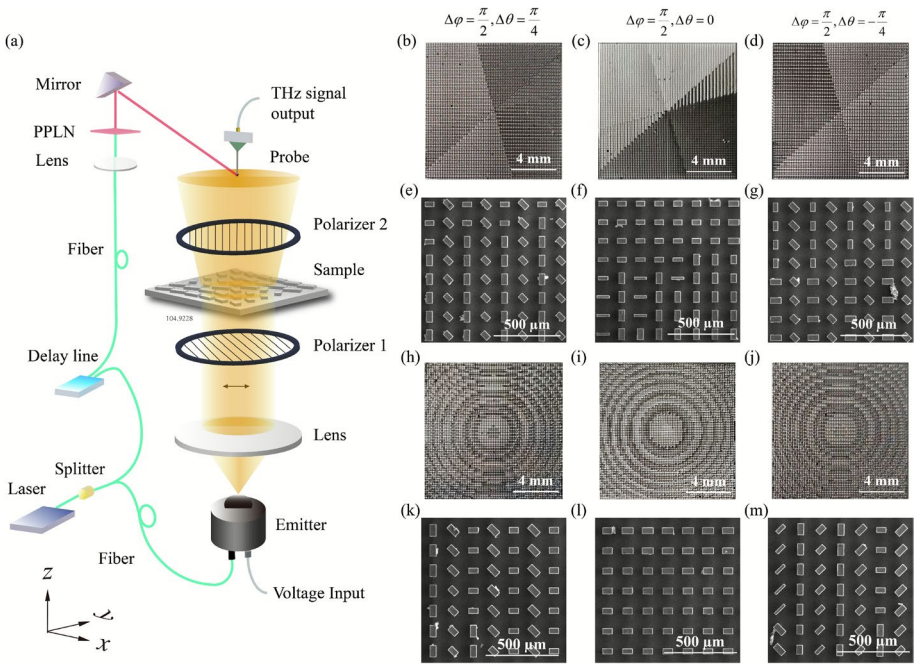

Fig. 3 The schematic of the terahertz field scanning microscope and sample images. **a** The schematic of the terahertz field scanning microscopy. PPLN is a periodically poled lithium niobate crystal used for frequency doubling. Two polarizers are applied to realize the full polarization measurement. **b** to **d** Optical images of spin-selective vortex beam generators with $\Delta\varphi = \pi/2$ and $\Delta\theta = \pi/4$ (**b**), $\Delta\varphi = \pi/2$ and $\Delta\theta = 0$ (**c**), and $\Delta\varphi = \pi/2$ and $\Delta\theta = -\pi/4$ (**d**), respectively. **e** to **g** The corresponding SEM images of fabricated microstructures for spin-selective vortex beam generators. **h** to **j** Optical images of spin-selective lenses with $\Delta\varphi = \pi/2$ and $\Delta\theta = \pi/4$ (**h**), $\Delta\varphi = \pi/2$ and $\Delta\theta = 0$ (**i**), and $\Delta\varphi = \pi/2$ and $\Delta\theta = -\pi/4$ (**j**), respectively. **k** and **m** The corresponding SEM images of the spin-selective lenses, respectively

and 10 mm for the spin-selective lenses, respectively. Figures 3k to m illustrate the corresponding SEM images of fabricated microstructures for spin-selective lenses. For the spin-selective vortex beam generator with $\Delta\phi = \varpi/2$ and $\Delta\vartheta = \varpi/4$, the electric field distributions that are captured by the terahertz field microscopy illustrate a donut-like intensity and encircle clockwise one time of 2π in the azimuth in the LCP − RCP component, while the other components vanish, as shown in Fig. 4c and d, agreeing well with the numerical results in Fig. 4a and b. We calculate the measured spin conversion efficiencies of the RCP to LCP channel (LCP − RCP component) and LCP to RCP channel (RCP − LCP component) by $\eta_{12} = \sum |E_{12}|^2 / \sum |E_{inc}|^2 \times 100\%$ and $\eta_{21} = \sum |E_{21}|^2 / \sum |E_{inc}|^2 \times 100\%$, respectively. $|E_{12}|^2$, $|E_{21}|^2$ and $|E_{inc}|^2$ represent the measured electric field intensities of the LCP − RCP component, RCP − LCP component, and incident beam, respectively. The corresponding measured spin conversion efficiencies are $\eta_{12} = 50.1\%$ and $\eta_{21} = 1.8\%$, respectively. By changing the orientation angles

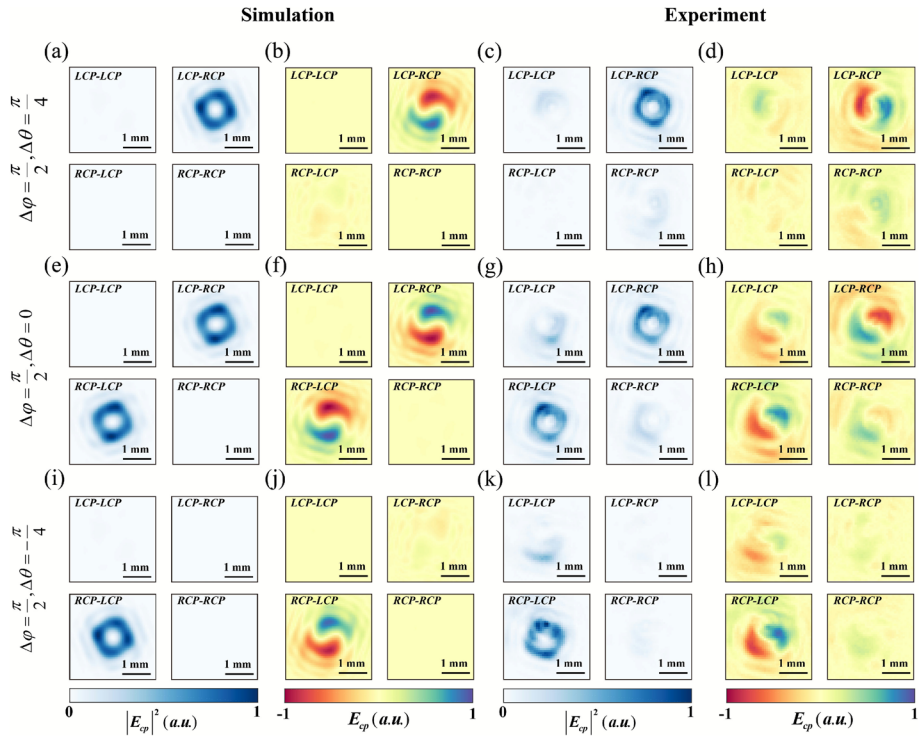

Fig. 4 Numerical and experimental results of spin-selective vortex beam generators. **a** and **b** Numerical results of the electric field intensity ($|E_{cp}|^2$) and electric field (E_{cp}) distributions for a spin-selective vortex beam generator with $\Delta\varphi = \pi/2$ and $\Delta\theta = \pi/4$ respectively. Only the LCP − RCP component shows a donut-like intensity distribution (**a**) and encircles one time of 2π in the azimuth (**b**). **c** and **d** The corresponding experimental results of the spin-selective vortex beam generator with $\Delta\varphi = \pi/2$ and $\Delta\theta = \pi/4$, respectively. **e** and **f** Numerical results of the intensity and electric field distributions for a spin-selective vortex beam generator with $\Delta\varphi = \pi/2$ and $\Delta\theta = 0$, respectively. There are vortex beams in both LCP − RCP and LCP − RCP components. **g** and **h** The corresponding experimental results of the spin-selective vortex beam generator with $\Delta\varphi = \pi/2$ and $\Delta\theta = 0$, respectively. **i** and **j** Numerical results of the electric field intensity and electric field distributions for a spin-selective vortex beam generator with $\Delta\varphi = \pi/2$ and $\Delta\theta = -\pi/4$, respectively. Different from **a** and **b**, only the RCP − LCP component illustrates a donut-like intensity distribution and encircles one time of 2π in the azimuth, respectively. **k** and **l** The corresponding experimental results of the spin-selective vortex beam generator with $\Delta\varphi = \pi/2$ and $\Delta\theta = -\pi/4$, respectively. $|E_{cp}|^2$ represents the electric field intensity of the LCP or RCP

between pillars of elements from $\Delta\theta = \pi/4$ to $\Delta\theta = 0$, it leads to a normal vortex beam generator that both LCP − RCP and RCP − LCP components can generate vortex beams, as shown in Fig. 4e and f. The measured intensity field distributions illustrate the donut-like intensity in both LCP − RCP and RCP − LCP components, with nearly uniform amplitude across the ring, as shown in Fig. 4g. Meanwhile, in Fig. 4h, the electric field encircles clockwise one time of 2π in the azimuth in both LCP − RCP and RCP − LCP components, agreeing well with the numerical results in Fig. 4f. The corresponding measured spin conversion efficiencies are $\eta_{12} = 26.0\%$ and $\eta_{21} = 26.6\%$, respectively. For a spin-selective vortex beam generator with $\Delta\varphi = \pi/2$ and $\Delta\theta = -\pi/4$, the eigenvalues and eigenvectors of the transmission matrix of the compound unit cells coalesce, leading the corresponding eigenvectors locating at the south pole of the Poincaré sphere. The spin-selective vortex beam generator implements solely conversion from LCP to RCP. The numerical and measured results depict a donut-like intensity in the RCP − LCP component in the intensity field distributions, and illustrate clockwise encircling one time of 2π in the azimuth in the RCP − LCP component in the electric field distributions, as depicted in Fig. 4i and l, respectively. The corresponding measured spin conversion efficiencies are $\eta_{12} = 2.10\%$ and $\eta_{21} = 50.2\%$, respectively.

Figure 5c and d show the measured intensity distributions of a metasurface lens with $\Delta\varphi = \pi/2$ and $\Delta\theta = \pi/4$ at the focal plane ($z = 10$ mm) and along the propagation direction ($y = 0$ mm), which agrees with the numerical results in Fig. 5a and b, respectively. As expected, the focusing behavior is solely observed in the LCP − RCP component. In contrast, when a metasurface lens is designed with $\Delta\varphi = \pi/2$ and $\Delta\theta = 0$, the transmitted beams in both LCP − RCP and RCP − LCP components are focused on the location of $z = 10$ mm, with an intensity ratio of approximately 1:1, as shown in Fig. 5e, respectively. The measured spin conversion efficiencies are $\eta_{12} = 27.5\%$ and $\eta_{21} = 26.6\%$, respectively. The measured intensity ratio is approximately 1.03:1 as illustrated in Fig. 5g, agreeing well with simulation results in Fig. 5e (See Note 2). The focusing behavior can be manipulated to emerge solely in the RCP − LCP component by simply building the spin-selective lens with $\Delta\varphi = \pi/2$ and $\Delta\theta = -\pi/4$. The measured intensity distributions at the focal plane and the propagation plane in Fig. 5k and l agree well with the numerical results in Fig. 5i and j, respectively.

Generally, a genuinely non-Hermitian system originates from intrinsic physical mechanisms, such as gain, loss, or non-reciprocal asymmetric coupling, which introduces a fundamentally non-Hermitian operator. While the governing Hamiltonian of our system is entirely Hermitian (no gain/loss, non-reciprocity), the Jones matrix only concerns part of the system, which describes the parameter space associated with input and output light. In this case, as the sub-system can exchange energy with the rest of the system, EPs can emerge in parameter regions where the eigenvalues and eigenvectors of the system's governing scattering matrix coalesce, a phenomenon that has also been observed in other systems with asymmetrical backscattering [47] and Hermitian systems [1]. In our work, the Jones matrix of a compound unit cell describes the interference between orthogonal spin channels (LCP ↔ RCP). By tuning the sizes and rotation angles of the two consistent dielectric pillars, the eigenvalues and eigenvectors of the Jones matrix associated with the compound unit cell coalesce, thereby giving rise to an EP in the parameter space (See Note 3). Notably, in our system the eigenvalues correspond to

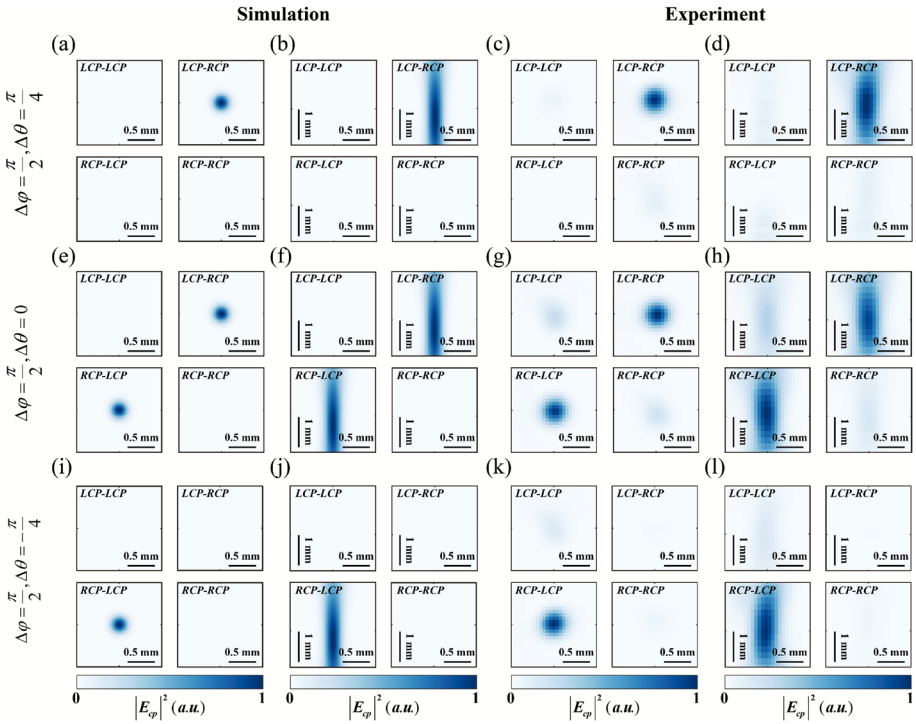

Fig. 5 Numerical and experimental results of spin-selective lenses. **a** and **b** Numerical results of the electric field intensity distributions in the focal plane and propagation plane of the spin-selective lenses with $\Delta\varphi = \pi/2$ and $\Delta\theta = \pi/4$, respectively. Only the transmitted beam in the LCP − RCP component is focused as expected. **c** and **d** The corresponding experimental results of the spin-selective lenses with $\Delta\varphi = \pi/2$ and $\Delta\theta = \pi/4$, respectively. **e** and **f** Numerical results of the electric field intensity distributions in the focal plane and propagation plane of the spin-selective lenses with $\Delta\varphi = \pi/2$ and $\Delta\theta = 0$, respectively. Both the LCP − RCP and RCP − LCP components focus light at a distance of z = 10 mm, with an intensity ratio of approximately 1:1. **g** and **h** The corresponding experimental results of the spin-selective lenses with $\Delta\varphi = \pi/2$ and $\Delta\theta = 0$, respectively. **i** and **j** Numerical results of the electric intensity distributions in the focal plane and propagation plane of the spin-selective lenses with $\Delta\varphi = \pi/2$ and $\Delta\theta = -\pi/4$, respectively. Only the transmitted beam in the RCP-LCP component is focused at $z = 10$ mm. **k** and **l** The corresponding experimental results of the spin-selective lenses with $\Delta\varphi = \pi/2$ and $\Delta\theta = -\pi/4$, respectively

complex transmission amplitudes and the eigenvectors represent the associated polarization states. This differs from a genuinely non-Hermitian system, where the eigenvalues typically represent complex frequencies or energies and the eigenvectors correspond to physical modes supported by the structure.

Conclusion

We propose and experimentally demonstrate a method to construct EPs in the parameter space without complex couplings within a unit cell, enabling suppression of residual zero-order diffraction. By tailoring the sizes and relative orientations of the two dielectric pillars within a compound unit cell, EPs emerge from the superposition of the accumulated geometric and propagation phases of the two constituent pillars, resulting in the formation of nodal lines consisting of EPs in the parameter space. By selecting parameters of the compound unit cell along nodal lines, the dielectric metasurfaces can realize solely spin conversion. Using terahertz imaging techniques, we experimentally implement spin-selective terahertz lenses and vortex beam generators, with the

measured results exhibiting good agreement with numerical simulations. Constructing optical elements using compound unit cells that support EPs in the transmission matrix offers new insights into building intriguing optical elements for both linear and nonlinear electromagnetic field control.

Methods

Material and fabrication

The silicon is selected due to its low absorption in the terahertz regime, whose refractive index is 3.4. The metasurfaces are fabricated on the 1.5-mm-thick silicon substrate. Fabrication of the metasurface can be classified into three steps: first, the micro-column patterns are defined by E-beam lithography after the silicon wafer is spin-coated with a 10-μm-thick photoresist. Next, deep reactive ion etching is applied to make the silicon pillars with a height of 200 μm. Finally, the silicon wafer is cleaned with an acetone solution and DI water.

Measurement

In the measurement, the electric field was scanned using terahertz microscopy with a 0.2 mm step size from − 4 mm to 4 mm along both the x- and y-directions (See Note 2). The probe was placed approximately 12 mm above the surface of the samples to detect the spin-selective vortex generator. For the samples to realize spin-selective lenses, the probe was placed ~ 10 mm (focal plane) above the surface of the samples. The electric field was scanned with a 0.06 mm step from − 0.78 mm to 0.78 mm in both the x- and y-directions. The propagation plane was scanned with a 0.2 mm step from 8.8 mm to 11.6 mm in the z-direction and a 0.06 mm step from − 0.78 mm to 0.78 mm in the x-direction. Meanwhile, the working frequency was shifted to 1.15 THz, which might be the result of the shorter etching time, leading to the height of the pillar being smaller than designed.

Numerical simulation

The response of the dielectric pillar is simulated in the CST Microwave Studio (Computer Simulation Technology GmbH, Darmstadt, Germany). In the simulation, the periodic boundary condition is applied in both the x- and y-directions. The open boundary condition is applied in the z-direction. The period of an element along the x- and y-directions is 280 μm and 140 μm, respectively. The height of an element is 200 μm. The amplitude and phase responses are acquired by sweeping the length a_1 and width b_1 of the element at 1 THz under x- and y-polarized incidence, respectively. To meet the simplification condition, elements are selected by the criterion $\Delta A \leq 0.05$, and $|\varphi_x(x,y) - \varphi_y(x,y)| < \pi \pm \pi/36$. The metasurfaces are composed of 80×80 elements. The electric field distributions are calculated with the home-built MATLAB codes. The Rayleigh-Sommerfeld diffraction formula in the main text is as follows,

$$U(x_0, y_0) = \frac{1}{i\lambda} \iint U(x,y) cos < \boldsymbol{n}, \boldsymbol{r} > \frac{exp(ikr)}{r} dxdy \tag{2}$$

Where $U(x_0, y_0)$ and $U(x,y)$ are the electric fields on the image plane and the object plane, respectively. λ and k are the working wavelength and wave number in vacuum,

respectively. r is the distance between the pixel in the image plane and that in the object plane:$r = \sqrt{(x_0 - x)^2 + (y_0 - y)^2 + z^2}$; $cos < \boldsymbol{n}, \boldsymbol{r} >= \frac{z}{r}$ is the inclination factor.

Abbreviations

EP Exceptional point
LCP Left-handed circular polarization
RCP Right-handed circular polarization
CST Computer Simulation Technology

Supplementary Information

The online version contains supplementary material available at https://doi.org/10.1186/s43074-026-00226-6.

Supplementary Material 1.

Acknowledgements
Yang Long gratefully acknowledges the support of the Eric and Wendy Schmidt AI in Science Postdoctoral Fellowship, a Schmidt Futures program.

Authors' contributions
M. W., G.-G. L., and Y. L. initiated the idea. M. W. performed the numerical calculation. M. W. designed the experiments. S. H. characterized the samples. M. W. carried out the measurements and analyzed the data. M. W. , G.-G. L., Y. L., Z. C., S. H., S. M., and B. Z. wrote the manuscript. B. Z. supervised the project.

Funding
This research is supported by the Singapore National Research Foundation Competitive Research Program (Grant No. NRF-CRP23-2019–0007) and the Singapore Ministry of Education Academic Research Fund Tier 2 (Grant No. MOE-T2EP50123-0007). S. H. acknowledges the National Key R&D Program of China (2024YFB2808200), the National Natural Science Foundation of China (62475230), the Excellent Young Scientists Fund Program (Overseas) of China, and the Fundamental Research Funds for the Central Universities. G.-G. L. acknowledges funding from Research Center for Industries of the Future (RCIF) at Westlake University grant no. 210000006022312 and Westlake Education Foundation grant no. 103110736022301.

Data availability
The data that support the plots within this paper are available from the corresponding author upon reasonable request.

Declarations

Ethics approval and consent to participate
All authors participate in this work and the manuscript.

Consent for publication
All authors agreed to publish this paper.

Competing interests
The authors declare no competing interests.

Received: 3 August 2025 Revised: 10 December 2025 Accepted: 2 January 2026
Published online: 13 January 2026

References

1. Miri M-A, Alù A. Exceptional points in optics and photonics. Science. 2019;363:eaar7709.
2. Özdemir ŞK, Rotter S, Nori F, Yang L. Parity–time symmetry and exceptional points in photonics. Nat Mater. 2019;18:783–98.
3. Wiersig J. Review of exceptional point-based sensors. Photon Res. 2020;8:1457.
4. Ding K, Fang C, Ma G. Non-hermitian topology and exceptional-point geometries. Nat Rev Phys. 2022;4:745–60.
5. Zhen B, et al. Spawning rings of exceptional points out of Dirac cones. Nature. 2015;525:354–8.
6. Huang Y, Shen Y, Min C, Fan S, Veronis G. Unidirectional reflectionless light propagation at exceptional points. Nanophotonics. 2017;6:977–96.
7. Rüter CE, et al. Observation of parity–time symmetry in optics. Nat Phys. 2010;6:192–5.
8. Wang C, Sweeney WR, Stone AD, Yang L. Coherent perfect absorption at an exceptional point. Science. 2021;373:1261–5.
9. Wang C, et al. Electromagnetically induced transparency at a chiral exceptional point. Nat Phys. 2020;16:334–40.
10. Chen W, Kaya Özdemir Ş, Zhao G, Wiersig J, Yang L. Exceptional points enhance sensing in an optical microcavity. Nature. 2017;548:192–6.
11. Mao W, Fu Z, Li Y, Li F, Yang L. Exceptional–point–enhanced phase sensing. Sci Adv. 2024;10:eadl5037.

12. Park J-H, et al. Symmetry-breaking-induced plasmonic exceptional points and nanoscale sensing. Nat Phys. 2020;16:462–8.
13. Ferise C, Del Hougne P, Félix S, Pagneux V, Davy M. Exceptional points of P T -symmetric reflectionless states in complex scattering systems. Phys Rev Lett. 2022;128:203904.
14. Yu N, et al. Light propagation with phase discontinuities: generalized laws of reflection and refraction. Science. 2011;334:333–7.
15. Kildishev AV, Boltasseva A, Shalaev VM. Planar photonics with metasurfaces. Science. 2013;339:1232009.
16. Hsiao H, Chu CH, Tsai DP. Fundamentals and applications of metasurfaces. Small Methods. 2017;1:1600064.
17. Kamali SM, Arbabi E, Arbabi A, Faraon A. A review of dielectric optical metasurfaces for wavefront control. Nanophotonics. 2018;7:1041–68.
18. Chen WT, Zhu AY, Capasso F. Flat optics with dispersion-engineered metasurfaces. Nat Rev Mater. 2020;5:604–20.
19. Chen S, Liu W, Li Z, Cheng H, Tian J. Metasurface-empowered optical multiplexing and multifunction. Adv Mater. 2020;32:1805912.
20. Zhao R, Huang L, Wang Y. Recent advances in multi-dimensional metasurfaces holographic technologies. PhotoniX. 2020;1:20.
21. Hu Y, et al. Dielectric metasurface zone plate for the generation of focusing vortex beams. PhotoniX. 2021;2:10.
22. Chen Q, et al. Metasurface-engineered thermal emitters enabled chip-scale mid-infrared spectroscopic sensing. PhotoniX. 2025;6:19.
23. Yuan Q, et al. Scalable high-efficiency metasurface-refractive retro-reflector. PhotoniX. 2025;6:14.
24. Jang J, et al. Wavelength-multiplexed orbital angular momentum meta-holography. PhotoniX. 2024;5:27.
25. Cong L, et al. A perfect metamaterial polarization rotator. Appl Phys Lett. 2013;103:171107.
26. Wu Z, Ra'di Y, Grbic A. Tunable metasurfaces: a polarization rotator design. Phys Rev X. 2019;9:011036.
27. Ding F, Wang Z, He S, Shalaev VM, Kildishev AV. Broadband high-efficiency half-wave plate: a supercell-based plasmonic metasurface approach. ACS Nano. 2015;9:4111–9.
28. Karimi E, et al. Generating optical orbital angular momentum at visible wavelengths using a plasmonic metasurface. Light Sci Appl. 2014;3:e167–e167.
29. Li G, et al. Spin-enabled plasmonic metasurfaces for manipulating orbital angular momentum of light. Nano Lett. 2013;13:4148–51.
30. Pfeiffer C, Grbic A. Bianisotropic metasurfaces for optimal polarization control: analysis and synthesis. Phys Rev Appl. 2014;2:044011.
31. Song Q, Odeh M, Zúñiga-Pérez J, Kanté B, Genevet P. Plasmonic topological metasurface by encircling an exceptional point. Science. 2021;373:1133–7.
32. Kang M, Chen J, Chong YD. Chiral exceptional points in metasurfaces. Phys Rev A. 2016;94:033834.
33. Leung HM, et al. Exceptional point-based plasmonic metasurfaces for vortex beam generation. Opt Express. 2020;28:503.
34. Park SH, et al. Observation of an exceptional point in a non-Hermitian metasurface. Nanophotonics. 2020;9:1031–9.
35. Kolkowski R, Kovaios S, Koenderink AF. Pseudochirality at exceptional rings of optical metasurfaces. Phys Rev Res. 2021;3:023185.
36. Wang X, Fang X, Mao D, Jing Y, Li Y. Extremely asymmetrical acoustic metasurface mirror at the exceptional point. Phys Rev Lett. 2019;123:214302.
37. Dong S, et al. Loss-assisted metasurface at an exceptional point. ACS Photon. 2020;7:3321–7.
38. Yang Z, et al. Asymmetric full-color vectorial meta-holograms empowered by pairs of exceptional points. Nano Lett. 2024;24:844–51.
39. Yi C, et al. Creating topological exceptional point by on-chip all-dielectric metasurface. Light Sci Appl. 2025;14:262.
40. Yang Z, et al. Creating pairs of exceptional points for arbitrary polarization control: asymmetric vectorial wavefront modulation. Nat Commun. 2024;15:232.
41. Qin H, et al. Sphere of arbitrarily polarized exceptional points with a single planar metasurface. Nat Commun. 2025;16:2656.
42. Overvig AC, et al. Dielectric metasurfaces for complete and independent control of the optical amplitude and phase. Light Sci Appl. 2019;8:92.
43. Lee G-Y, et al. Complete amplitude and phase control of light using broadband holographic metasurfaces. Nanoscale. 2018;10:4237–45.
44. Wu T, et al. Dielectric metasurfaces for complete control of phase, amplitude, and polarization. Adv Opt Mater. 2022;10:2101223.
45. Balthasar Mueller JP, Rubin NA, Devlin RC, Groever B, Capasso F. Metasurface polarization optics: independent phase control of arbitrary orthogonal states of polarization. Phys Rev Lett. 2017;118:113901.
46. Xu Y, et al. Spin-decoupled multifunctional metasurface for asymmetric polarization generation. ACS Photon. 2019;6:2933–41.
47. Chen J, et al. Coherent-resonance enhancement of sensing at the exceptional points. Adv Opt Mater. 2024;12:2302268.

Publisher's Note